Two-dimensional models of core-collapse supernova explosions assisted by heavy sterile neutrinos

Kanji Mori[1,*] Tomoya Takiwaki,[1] Kei Kotake,[2,3] and Shunsaku Horiuchi[4,5]

[1]*National Astronomical Observatory of Japan, 2-21-1 Osawa, Mitaka, Tokyo 181-8588, Japan*
[2]*Research Institute of Stellar Explosive Phenomena, and Department of Applied Physics,*
Fukuoka University, 8-19-1 Nanakuma, Jonan-ku, Fukuoka-shi, Fukuoka 814-0180, Japan
[3]*Institute for Theoretical Physics, University of Wrocław, 50-204 Wrocław, Poland*
[4]*Center for Neutrino Physics, Department of Physics, Virginia Tech, Blacksburg, Virginia 24061, USA*
[5]*Kavli IPMU (WPI), UTIAS, The University of Tokyo, Kashiwa, Chiba 277-8583, Japan*

Core-collapse supernovae can be a copious source of sterile neutrinos, hypothetical particles that mix with active neutrinos. We develop two-dimensional stellar core-collapse models that incorporate the mixing between tau neutrinos and heavy sterile neutrinos—those with the mass of 150–200 MeV—to investigate signatures of sterile neutrinos in supernova observables. We find that the decay channel of a sterile neutrino into a pion and a tau neutrino can enhance the explosion energy and the synthesized nickel mass. Although the inclusion of sterile neutrinos considered in this study slightly reduce the neutrino and gravitational-wave signals, we find that they are still detectable for a Galactic event. Furthermore, we point out that if sterile neutrinos are as massive as ∼200 MeV, they produce high-energy tau antineutrinos with energies of ∼80 MeV, the detection of which can be a smoking signature of the sterile neutrinos and where Hyper-Kamiokande should play a pivotal role.

I. INTRODUCTION

In the Standard Model of particle physics, neutrinos are treated as massless left-handed fermions. However, observations of neutrino oscillations [e.g., [1,2]] reveal that the neutrino masses are nonzero. Although the origin of the neutrino masses is under debate, introducing heavy right-handed particles called sterile neutrinos [3,4] naturally leads to finite masses of active neutrinos through the seesaw mechanism [5–7].

Apart from the theoretical motivation above, there are experimental hints of sterile neutrinos. For example, electron antineutrino fluxes from reactors are anomalously smaller than theoretical expectations [8–10]. This deficit could be explained by oscillations into sterile neutrinos [11]. Also, sterile neutrinos with mass ∼keV work as a candidate of dark matter [12–14]. Interestingly, x-ray observations of galaxy clusters and galaxies with the XMM–Newton and Chandra satellites detected a 3.5 keV line, which can be interpreted as a signature of the radiative decay of 7.1 keV-mass sterile neutrino dark matter [15–17]. Although the sterile neutrino interpretation for these signatures is under debate [e.g., [10,14,18–23]], these studies motivate experimental and astronomical explorations of the particle.

Core-collapse supernovae are a useful laboratory for sterile neutrinos because neutrinos play essential roles in the supernova explosion mechanism. Sterile neutrinos can be produced in supernova events through mixing with active neutrinos and can affect the energy transfer inside. Indeed, the effects of sterile neutrinos on supernovae have been investigated for various sterile neutrino masses $m_s = \mathcal{O}(\text{eV})$ [24–34], $\mathcal{O}(\text{keV})$ [35–46], and $> \mathcal{O}(\text{MeV})$ [47–54]. Although these studies have gradually refined the microphysics, they nonetheless have only adopted spherically symmetric supernova models. This is despite the fact that, multidimensionality is essential to the supernova explosion mechanism. Also, it is not possible to predict gravitational wave signals with one-dimensional models. In this study, we hence develop two-dimensional supernova models coupled with sterile neutrinos.

We focus on a heavy sterile neutrino model with $m_s = 150$–200 MeV and Lagrangian [48,52],

$$\mathcal{L} = \mathcal{L}_{\text{SM}} + i\bar{\nu}_s \slashed{\partial}\nu_s - y_\nu \bar{L}\,\tilde{H}\,\nu_s + \frac{m_s}{2}\bar{\nu}_s^c \nu_s + \text{H.c.}, \quad (1)$$

where $\mathcal{L}_{\text{SM}}$ is the Standard Model Lagrangian, y_ν is a Yukawa coupling constant, H is the $\text{SU}(2)_L$ Higgs doublet, and L is the lepton doublet. The Yukawa coupling term leads to a Dirac mass term below the electroweak scale and diagonalization of the Dirac and Majorana mass terms

[*]Contact author: kanji.mori@nao.ac.jp
Research Fellow of Japan Society for the Promotion of Science.

023031-1

provides the masses of active and sterile neutrinos through the seesaw mechanism. We assume that sterile neutrinos mix with ν_τ,

$$\nu_\tau = \cos\theta_{\tau 4}\nu_1 + \sin\theta_{\tau 4}\nu_2$$
$$\nu_s = -\sin\theta_{\tau 4}\nu_1 + \cos\theta_{\tau 4}\nu_2, \qquad (2)$$

where ν_1 and ν_2 are the mass eigenstates and $\theta_{\tau 4}$ is the mixing angle. Heavy sterile neutrinos that mix with ν_e and ν_μ have been strongly excluded by terrestrial experiments [55–57], but mixing with ν_τ is less constrained. Core-collapse supernovae can provide a unique way to constrain the mixing angle $\theta_{\tau 4}$ between ν_τ and ν_s. Such a constraint has been set from SN 1987A [48,51]. If sterile neutrinos exist, they can freely escape from the proto-neutron star and lead to an additional energy loss. Since this would affect the neutrino signals observed from SN 1987A, the mixing angle should be $\sin^2\theta_{\tau 4} \lesssim 2 \times 10^{-6}$ for $m_s = 200$ MeV [48,51]. In our simulations, we adopt sterile neutrino parameters that do not violate this constraint based on SN 1987A energy-loss argument.

This paper is organized as follows. In Sec. II, we explain our method to implement the transport of sterile neutrinos in supernova simulations. In Sec. III, we show the results of our simulations and discuss the effect of sterile neutrinos. In Sec. IV, we summarize and discuss the implication of our results. Throughout, we use natural units with $\hbar = c = k = G = 1$, where $\hbar$ is the Planck constant, c is the speed of light, k is the Boltzmann constant, and G is the gravitational constant.

II. METHOD

In this work, we consider a sterile neutrino model proposed in Ref. [48]. In a supernova core, a heavy sterile neutrino ν_s is produced by the pair annihilation of ν_μ and ν_τ. The processes considered in our calculation is tabulated in Refs. [48,51]. Although the annihilation processes of ν_e-$\bar{\nu}_e$ pairs and electron-positron pairs can produce ν_s as well, their contribution would be subdominant because these species are degenerate in the supernova core. We adopt the numerical result in Ref. [48] for the cooling rate induced by the sterile neutrino production,

$$Q_{\text{cool}} = 3 \times 10^{34} \text{ erg cm}^{-3} \text{ s}^{-1}$$
$$\times \left(\frac{\sin^2\theta_{\tau 4}}{5 \times 10^{-8}}\right)\left(\frac{T}{35 \text{ MeV}}\right)^{7.2} \exp\left(-\frac{m_s}{T}\right), \qquad (3)$$

where T is the temperature.

In this study, we explore sterile neutrino mass m_s of 150 and 200 MeV. This range of mass is particularly interesting because the sterile neutrino is heavier than the neutral pion, whose mass is $m_\pi \approx 135$ MeV [58]. In this case, the decay channel $\nu_s \to \nu_\tau\pi^0 \to \nu_\tau\gamma\gamma$ and its charge conjugate

reaction are kinematically allowed, and its lifetime can be estimated as [47,48,50]

$$\tau_s = \frac{16\pi}{G_F^2 m_s(m_s^2 - m_\pi^2)f_\pi^2\sin^2\theta_{\tau 4}}$$
$$\approx 66 \text{ ms}\left(\frac{\sin^2\theta_{\tau 4}}{5 \times 10^{-8}}\right)^{-1}\left(\frac{m_s}{200 \text{ MeV}}\right)^{-3}\left(\frac{0.54}{1 - \frac{m_\pi^2}{m_s^2}}\right), \qquad (4)$$

where G_F is the Fermi coupling constant and $f_\pi \approx 131$ MeV. If ν_s is heavier, other decay channels such as $\nu_s \to \nu_\tau\pi^+\pi^-$ would appear. These processes will shorten the lifetime of sterile neutrinos, but investigation of their effects is beyond the scope of this study.

In order to simulate the transport of sterile neutrinos, we solve the zeroth angular moment of the Boltzmann equation [50],

$$\frac{\partial\mathcal{E}}{\partial t} + \nabla\cdot\mathcal{F} = Q_{\text{cool}} - \kappa\mathcal{E}, \qquad (5)$$

where $\mathcal{E}$ is the ν_s energy per unit volume, $\mathcal{F}$ is the ν_s energy flux, and $\kappa = 1/\tau_s c$ is the opacity for the ν_s decay. We adopt the ray-by-ray approximation, in which the non-radial propagation of sterile neutrinos is not considered. We adopt $\mathcal{F} = c\mathcal{E}$ as the closure relation because sterile neutrinos only feebly interact with the surrounding material. The choice of the closure relation could be justified by the feeble interaction of sterile neutrinos. On the other hand, Ref. [50] adopts the two-moment method to solve the Boltzmann equation for sterile and active neutrinos. The nonlinear nature of the problem prevents one from predicting the consequences of different approximations. It is hence desirable to perform comparative studies on sterile neutrino transport methods, which are beyond the scope of this study.

When the density of the surrounding material is high enough, the active neutrinos produced by the sterile neutrino decay are absorbed locally and contribute to heating. On the other hand, when the density is low, the active neutrinos will freely escape. In this study, we follow the prescription in Ref. [50] to calculate the efficiency of the additional heating induced by sterile neutrino decay. If the density is higher than 10^{12} g cm^{-3}, the active neutrinos are assumed to be trapped and the heating rate is $Q_{\text{heat}} = \kappa\mathcal{E}$. When density is lower than 10^{10} g cm^{-3}, the heating rate is calculated as $Q_{\text{heat}} = \kappa\mathcal{E}x_{\gamma\gamma}$, where $x_{\gamma\gamma} = 0.5(1 + m_\pi^2/m_s^2)$. When the density is intermediate, Q_{heat} is linearly interpolated between the two regimes. Once Q_{cool} and Q_{heat} are obtained, sterile neutrinos are coupled with the hydrodynamics through

$$\left(\frac{\partial e_{\text{int}}}{\partial t}\right)_{\nu_s} = Q_{\text{heat}} - Q_{\text{cool}}, \qquad (6)$$

TABLE I. Parameters for the supernova models developed in this study and results. We adopt a "Standard" model without sterile neutrinos and six models with sterile neutrinos. Each of the latter models is designated by a pair of two integers that indicates the mass and mixing angle, i.e., (m_s [MeV], $\sin^2\theta_{\tau 4}/10^{-8}$). The fourth column shows the mean free path (MFP) of sterile neutrinos. The fifth column shows the post-bounce time $t_{pb,2000}$ at which the bounce shock reaches the radius 2000 km when angle averaged. The sixth column shows the diagnostic explosion energy defined in Eq. (8). The seventh column shows the synthesized nickel mass defined in Eq. (10). The eighth column shows the additional heating outside the simulated region based on Eq. (9). E_{diag}, M_{Ni}, M_{PNS}, and E_s are all evaluated at $t_{pb} = t_{pb,2000}$.

Model	m_s [MeV]	$\sin^2\theta_{\tau 4}$	MFP [10^4 km]	$t_{pb,2000}$ [ms]	E_{diag} [10^{51} erg]	$M_{Ni}[M_\odot]$	$M_{PNS}[M_\odot]$	E_s [10^{51} erg]
Standard	$\cdots$	0	$\cdots$	395	0.36	0.077	1.83	0
(150, 6)	150	6×10^{-8}	11.5	370	0.61	0.086	1.82	8.77
(150, 10)	150	1×10^{-7}	6.92	360	0.76	0.084	1.82	12.2
(150, 20)	150	2×10^{-7}	3.46	321	2.02	0.089	1.80	15.3
(200, 6)	200	6×10^{-8}	1.64	362	0.59	0.088	1.82	1.64
(200, 10)	200	1×10^{-7}	0.99	345	0.87	0.085	1.81	1.85
(200, 20)	200	2×10^{-7}	0.49	316	2.26	0.105	1.78	1.66

where $\left(\frac{\partial e_{int}}{\partial t}\right)_{\nu_s}$ is the contribution of ν_s in the source term of the energy equation.

We implement the transfer of sterile neutrinos described above in the 3DnSNe code [59] to simulate the stellar core collapse with axisymmetric geometry. The transfer of active neutrinos is treated with a three-flavor isotropic diffusion source approximation [60–62]. We also solve the α network that includes 13 nuclei to consider the nuclear energy generation and nucleosynthesis [63]. We adopt the nuclear equation of state in Ref. [64] with $K = 220$ MeV. The spatial resolution of our two-dimensional simulations is $n_r \times n_\theta = 512 \times 128$. The simulated region is a sphere with the radius of 5000 km. The progenitor model is the nonrotating $20M_\odot$ solar metallicity star in Ref. [65].

III. RESULTS

In this work, we develop six models with sterile neutrinos and one model without sterile neutrinos (the "Standard" model). The ν_s mass is assumed to be 150 or 200 MeV and the mixing angle is $\sin^2\theta_{\tau 4} = 6 \times 10^{-8}$, 1×10^{-7}, or 2×10^{-7}. The characteristics of the models are tabulated in Table I.

Note that while our chosen sterile neutrino parameters evade the constraint in Ref. [51] that is based on the supernova energy loss argument, they are in the excluded region based on the explosion energy of low-energy supernovae [52,53]. However, the explosion energy constraint is based on a post-process calculation of the sterile neutrinos' effects, and thus it is still worthwhile to investigate the dynamical effects of heavy sterile neutrinos in our numerical implementation.

In this section, we discuss the properties of our models. Each model is designated by a pair of two numbers, ($m_s/1$ MeV, $\sin^2\theta_{\tau 4}/10^{-8}$), throughout the paper.

A. Additional cooling and heating

Sterile neutrinos contribute to both cooling and heating in addition to the active neutrinos. Figure 1 shows the radial profile of Q_{cool} at the post-bounce time $t_{pb} = 0.2$ s. The cooling rate Q_{cool} reaches a peak at $r \approx 10$ km. This is because the temperature reaches the highest value, ~ 45 MeV, at this radius and Q_{cool} is very sensitive to the temperature as shown in Eq. (3). Figure 1 also shows the radial profile of Q_{heat}, which is obtained by solving Eq. (5). When the sterile neutrino mass and the radius are fixed, Q_{heat} is approximately proportional to $\sin^4\theta_{\tau 4}$ because both Q_{heat} and κ are proportional to $\sin^2\theta_{\tau 4}$.

Figure 1 also shows the net heating and cooling rate

$$Q_{active} = Q_{heat,active} - Q_{cool,active} \qquad (7)$$

induced by active neutrinos. Here the "Standard" model was used to estimate the Q_{active} profile. We can see that the gain radius, where cooling balances with heating, is located at $r \approx 53$ km at $t_{pb} = 0.2$ s. At this radius, the contribution of sterile neutrinos on heating and cooling is smaller than the contribution of active neutrinos. Hence, the gain radius is not affected by sterile neutrinos. In addition, the figure shows that Q_{cool} for $m_s = 200$ MeV is smaller than that for $m_s = 150$ MeV when the mixing angle is fixed. This is because of the Boltzmann factor in Eq. (3). The difference in Q_{heat} is, however, less significant. This can be attributed to the longer lifetime for lighter sterile neutrinos, which leads to a smaller opacity. We note that Q_{heat} in the models with $\sin^2\theta_{\tau 4} = 2 \times 10^{-7}$ reaches $\sim 1\%$ of $Q_{heat,active}$. The values are so high that they could significantly affect supernova dynamics.

In Fig. 2, we show the luminosity $L_s|_{r=500\ km}$ of sterile neutrinos evaluated at $r = 500$ km. When m_s is fixed, larger mixing angles lead to higher luminosities. When the mixing angle is fixed, the luminosities for the models with
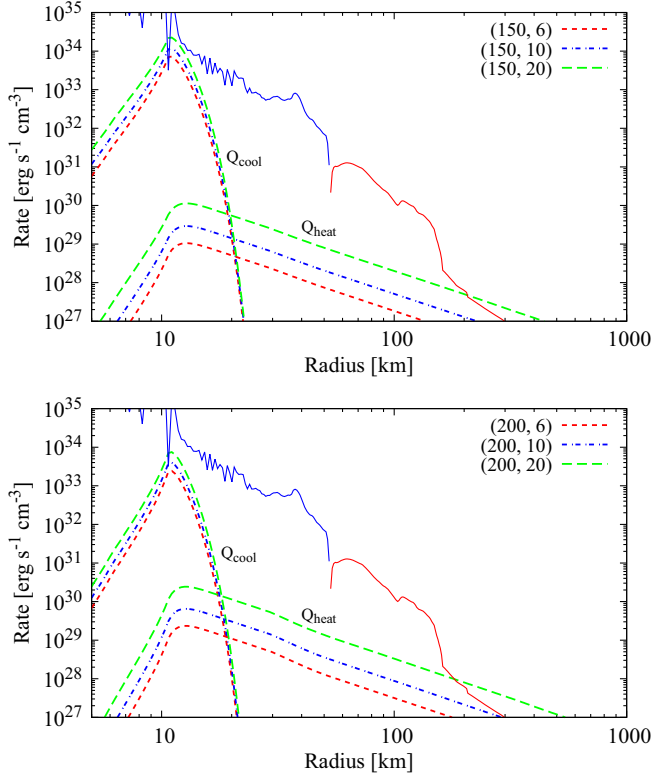
FIG. 1. The angular-averaged radial profile of the cooling rate Q_{cool} and the heating rate Q_{heat} induced by sterile neutrinos, with $m_{\mathrm{s}} = 150$ MeV (upper) and 200 MeV (lower) but different mixing angles. The solid lines indicate the net heating/cooling rate by active neutrinos, $|Q_{\mathrm{active}}|$, as defined in Eq. (7). Here the red and blue parts represent $Q_{\mathrm{active}} > 0$ and $Q_{\mathrm{active}} < 0$, respectively. All shown for $t_{\mathrm{pb}} = 0.2$ s.

$m_{\mathrm{s}} = 150$ MeV are ~3–4 times higher than those for the models with $m_{\mathrm{s}} = 200$ MeV, because the production of heavy sterile neutrinos is suppressed by the Boltzmann factor.
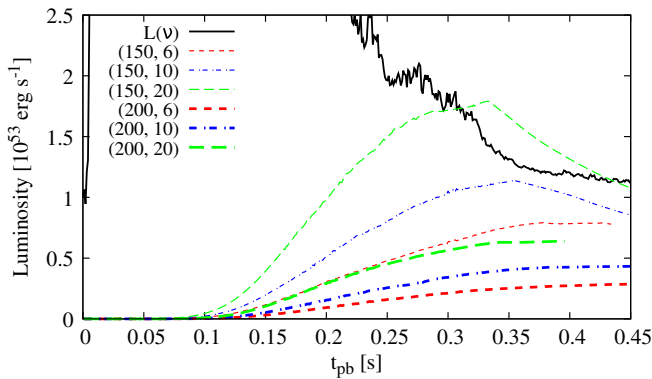
FIG. 2. The active neutrino luminosity (thick solid black) and the sterile neutrino luminosity $L_{\mathrm{s}}|_{r=500\ \mathrm{km}}$ (as labeled), all evaluated at $r = 500$ km as functions of t_{pb}. The thin lines are for the models with $m_{\mathrm{s}} = 150$ MeV while the thick lines are for the models with $m_{\mathrm{s}} = 200$ MeV. Different line styles represent different mixing angles.

Figure 2 also shows the total active neutrino luminosity for the Standard Model without sterile neutrinos, i.e., $L_{\nu} = L_{\nu_e} + L_{\bar{\nu}_e} + 4L_{\nu_X}$, which is also evaluated at $r = 500$ km. We can see that L_{s} is lower than L_{ν} in almost all models, with the exception of the (150, 20) model, which is our highest mixing angle model and also the mass is low enough so as to not be strongly Boltzmann suppressed. A secondary effect in the (150, 20) model is that the proto-neutron star cooling induced by the sterile neutrino production is so efficient that the temperature at the region where sterile neutrinos are produced is significantly lower. As a result, the sterile neutrino luminosity starts decreasing quickly from post-bounce time $t_{\mathrm{pb}} \sim 0.34$ s.

B. Explosion properties

The additional cooling and heating rates shown in Fig. 1 may significantly affect the explosion dynamics. Figure 3 shows the time evolution of the radius of the bounce shock. Since the models are two dimensional, even the Standard Model without sterile neutrinos achieves shock revival and a successful explosion is triggered. However, Fig. 3 shows that the additional heating induced by sterile neutrinos leads to faster expansion of the bounce shock.

The effect of the additional heating can be seen in the explosion energy as well. Figure 4 shows the diagnostic
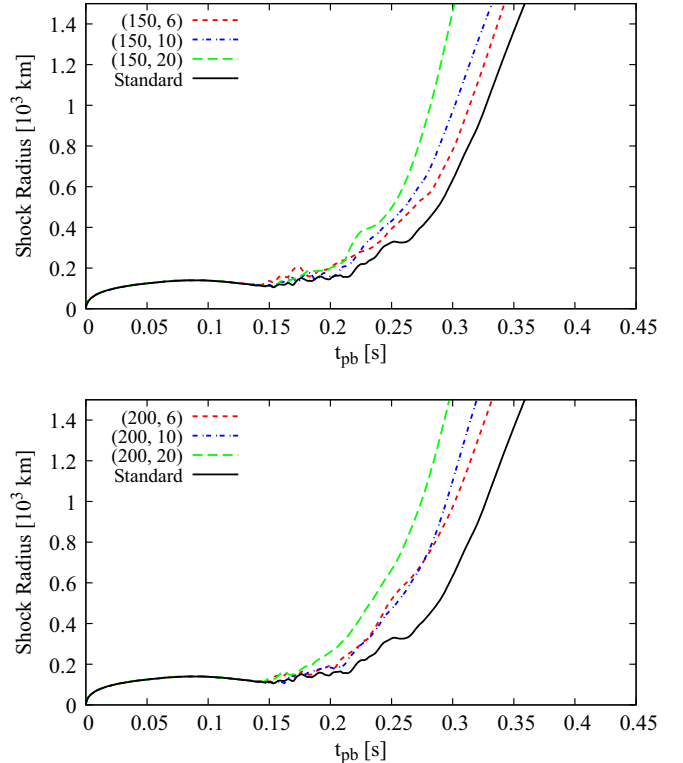

FIG. 3. The angle-averaged radius of the bounce shock as functions of post-bounce time t_{pb}. The upper panel is for the models with $m_{\mathrm{s}} = 150$ MeV and the lower panel is for $m_{\mathrm{s}} = 200$ MeV. The solid line shows the result for the Standard Model for comparison.

FIG. 4. The diagnostic energy of explosion E_{diag} as functions of post-bounce time t_{pb}. The upper panel is for the models with $m_s = 150$ MeV and the lower panel is for $m_s = 200$ MeV. The solid line shows the result for the Standard Model for comparison.
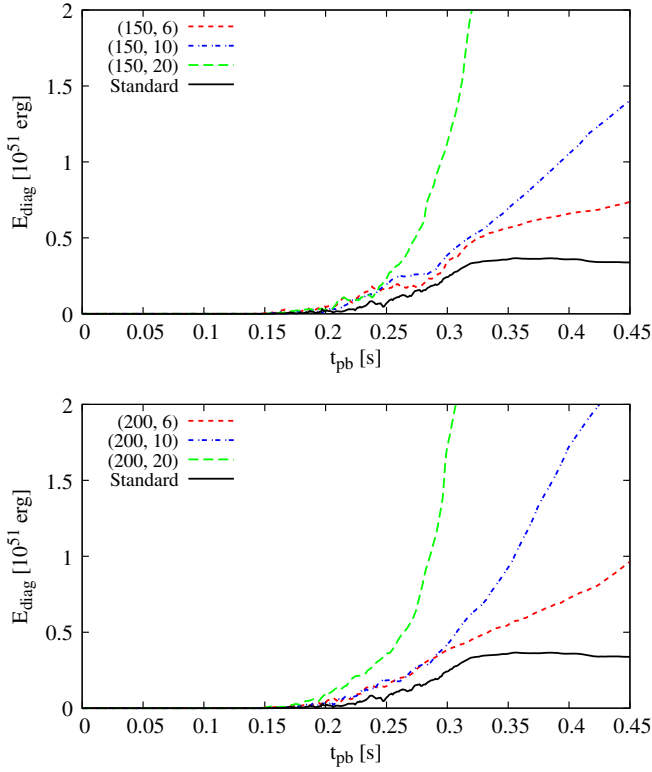
FIG. 5. The synthesized nickel mass M_{Ni} as a function of t_{pb}. The upper panel is for the models with $m_s = 150$ MeV and the lower panel is for the ones with $m_s = 200$ MeV. The solid line shows the result for the Standard Model and the others are for the models with sterile neutrinos.

energy of explosion defined as

$$E_{\text{diag}} = \int_D dV \left(\frac{1}{2}\rho v^2 + e - \rho\Phi \right), \qquad (8)$$

where ρ is the density, v is the velocity, e is the internal energy density, and Φ is the gravitational potential. The volume integral is performed in the region D where the integrand is positive and the radial velocity is outward. Whereas E_{diag} stalls at $\sim 0.4 \times 10^{51}$ erg in the Standard Model without sterile neutrinos, it continues to increase in the other models. Since Q_{heat} increases as a function of $\sin^2 \theta_{\tau 4}$, the explosion becomes more energetic when $\sin^2 \theta_{\tau 4}$ is larger. This is qualitatively consistent with the one-dimensional models of Ref. [50]. In particular, E_{diag} exceeds 1.5×10^{51} erg in the models with $\sin^2 \theta_{\tau 4} = 1 \times 10^{-7}$ and 2×10^{-7}. In these cases, the predicted explosion energy is higher than the most frequent value, 0.6×10^{51} erg, adopted for observed Type II supernovae [66]. This implies that the explosion energy is a useful observable to constrain the nature of sterile neutrinos [52,53,67].

It should be noted that the diagnostic energy of the explosion defined in Eq. (8) cannot be directly compared with observed explosion energies, because E_{diag} does not consider effects of the overburden and sterile neutrinos that decay outside the simulated region. The overburden reduces
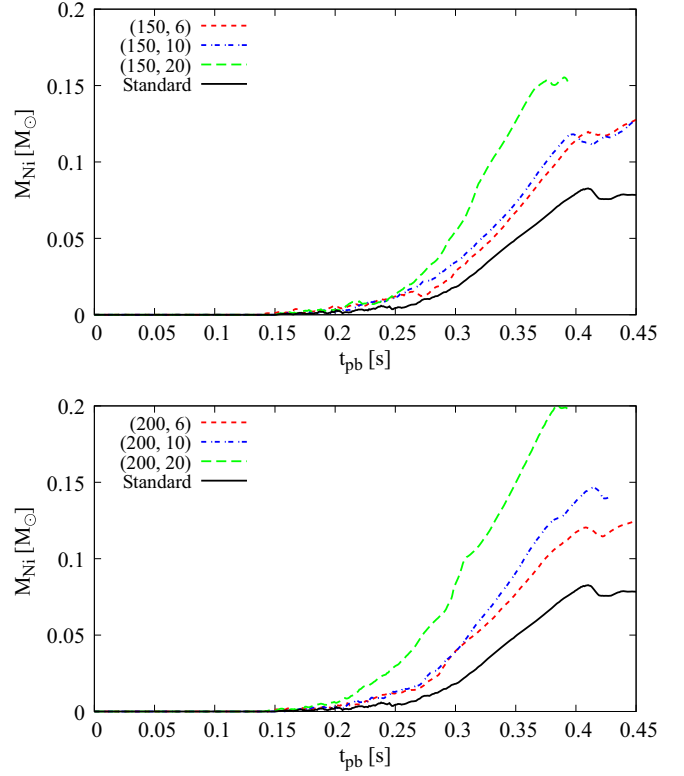
the explosion energy by $\sim (0.2-0.3) \times 10^{51}$ erg from the diagnostic energy when the shock radius is in the range of 2000–5000 km [68]. On the other hand, even if the decay happens outside the shock radius, it enhances the internal energy in the envelope and mitigates the overburden effect, leading to an enhancement of the asymptotic value for the explosion energy. The additional heating induced by sterile neutrinos which decay outside the simulated region enhances the explosion energy and can be estimated as

$$E_s = x_{\gamma\gamma} \int_0^t dt_{\text{pb}} L_s|_{r=5000 \text{ km}}, \qquad (9)$$

where $L_s|_{r=5000 \text{ km}}$ is the sterile neutrino luminosity at radius $r = 5000$ km. As shown in Table I, E_s is between $(2-20) \times 10^{51}$ erg, which is significantly larger than E_{diag}, in our parameter range. This implies that the explosion energy would grow beyond E_{diag} as the bounce shock propagates through the stellar envelope.

In Fig. 5 we show the ^{56}Ni mass,

$$M_{\text{Ni}} = \int_D dV X_{\text{Ni}} \rho, \qquad (10)$$

where X_{Ni} is the ^{56}Ni mass fraction and the volume integral is performed in the same region as the integral in Eq. (8).
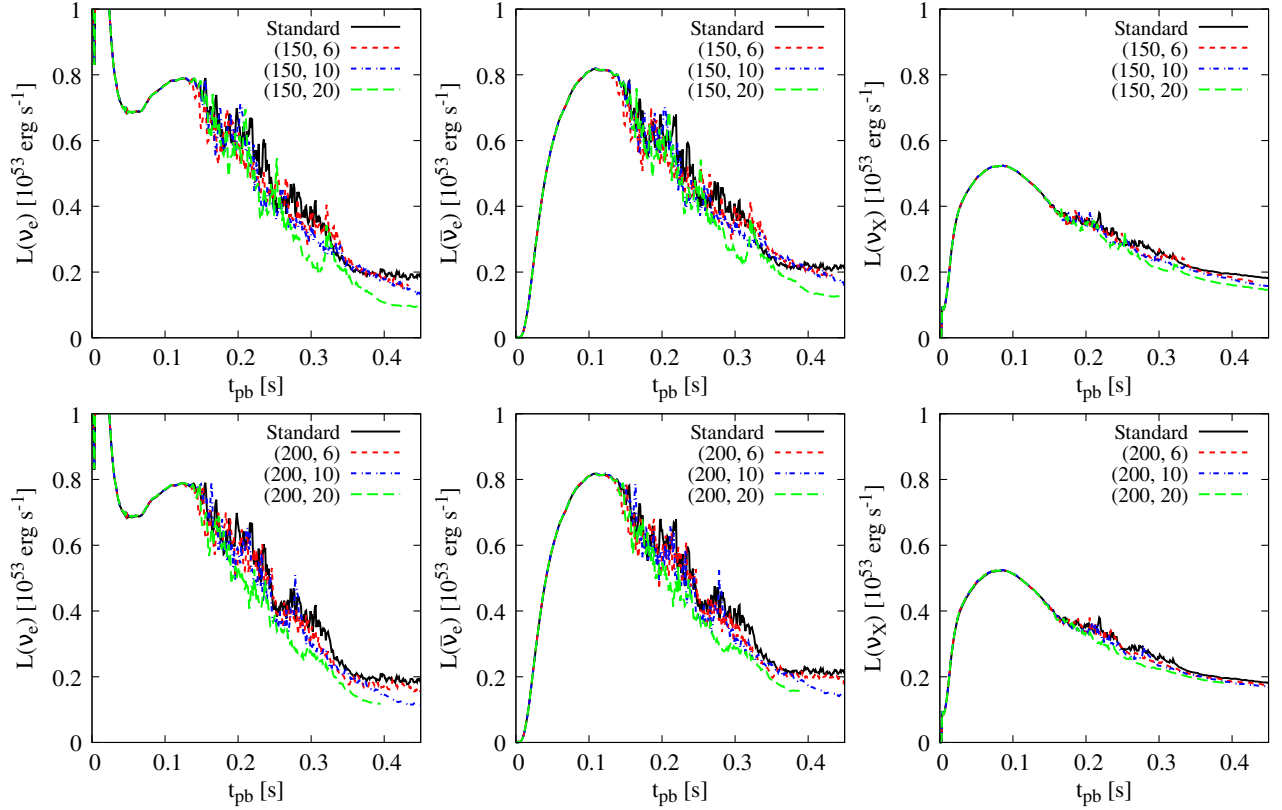
FIG. 6.   The luminosities of ν_e, $\bar{\nu}_e$, and ν_X as functions of t_{pb}. The contribution of decay (anti)neutrinos is not included. The upper panels are for the models with $m_s = 150$ MeV and the lower panels are for the ones with $m_s = 200$ MeV. The solid line shows the result for the "Standard" model and the others are for the models with sterile neutrinos.

The nickel mass saturates at $\sim 0.07 M_\odot$ in the Standard Model and becomes larger when the sterile neutrinos are considered. Nickel is mainly produced in the hot region where the temperature exceeds $\sim 5 \times 10^9$ K and complete silicon burning occurs [e.g., [69–72]]. Due to the additional heating induced by sterile neutrinos, the volume of the hot region becomes larger and the resultant nickel masses can exceed $0.1 M_\odot$.

One can estimate the nickel mass in supernova events from their light curves [73,74]. For example, the ejected nickel mass for SN 1987A is estimated to be $0.07 M_\odot$ [74]. Also, in a recent meta-analysis [75] on observational papers of Type II supernovae, the median of the nickel mass is estimated to be $0.032 M_\odot$ and the number of events with $M_{Ni} > 0.1 M_\odot$ is less than 10% of the total events. The comparison between these observations and our models implies that the models with $M_{Ni} > 0.1 M_\odot$ overproduce nickel, although it would be necessary to perform more systematic simulations for a wide range of stellar parameters to obtain a solid constraint on the sterile neutrino. Furthermore, we discuss the limitations of two-dimensional simulations in Sec IV.

C. Active neutrinos

The burst of active neutrino accompanying the core collapse can be detected by terrestrial detectors. The neutrino signal would provide information on the properties and dynamics in the collapsing core [e.g. [76,77]]. In particular, the energy transport induced by sterile neutrinos can affect the signals of active neutrinos.

Figure 6 shows the luminosity of active neutrinos, namely electron neutrinos, electron (anti)neutrinos, and heavy lepton neutrinos. Note that the active neutrinos produced in sterile neutrino decays are not included. One can see that the luminosities of all flavors decrease as a function of the mixing angle. This is because the mass accretion is suppressed by the additional heating induced by the sterile neutrino decay. Similar decrease of active neutrino luminosities has been reported in two-dimensional supernova models with axionlike particles [68] and QCD axions [78] as well.

Figure 7 shows the mean energy $\langle E \rangle$ of active neutrinos produced through the standard processes. Again, the active neutrinos produced in sterile neutrino decays are not included. Although the well-known hierarchy $\langle E(\nu_e) \rangle < \langle E(\bar{\nu}_e) \rangle < \langle E(\nu_X) \rangle$ is unchanged by sterile neutrinos, the absolute energies are affected by sterile neutrinos. The effect of sterile neutrinos is largely dependent on the sterile neutrino mass. When $m_s = 200$ MeV, the mean energies are lower than those in the Standard Model. This is because the temperature in the proto-neutron star is
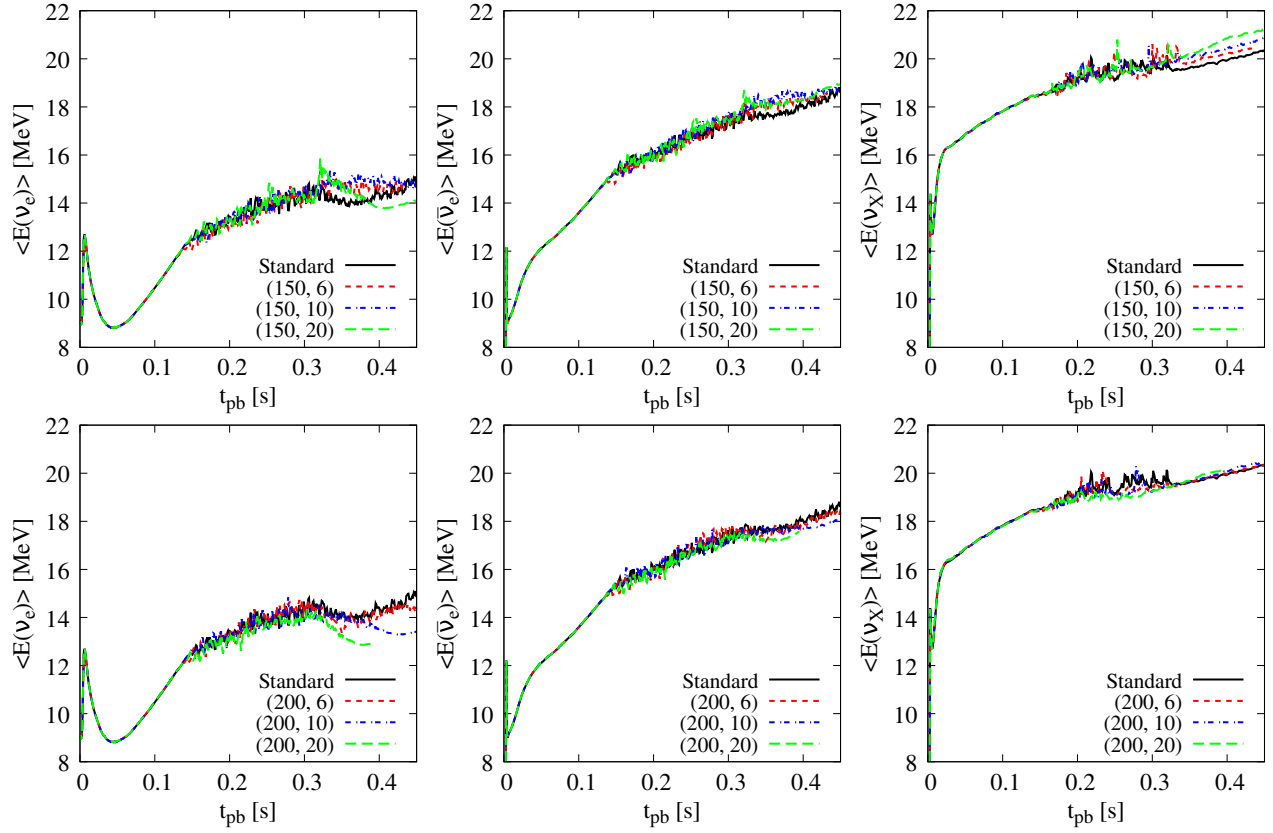
FIG. 7. The mean energies of ν_e, $\bar{\nu}_e$, and ν_X as a function of t_{pb}. The upper panels are for the models with $m_s = 150$ MeV and the lower panels are for the ones with $m_s = 200$ MeV. The solid line shows the result for the "Standard" model and the others are for the models with sterile neutrinos.

decreased by the additional cooling induced by the sterile neutrino production. This behavior is similar to the supernova models with axionlike particles [68]. On the other hand, when $m_s = 150$ MeV, the neutrino mean energies tend to become higher because of sterile neutrinos. This can be attributed to contraction of the proto-neutron star induced by the additional cooling effect. When the temperature is fixed, the sterile neutrino production rate is higher when sterile neutrinos are lighter because of the Boltzmann factor, as we can see in Eq. (3). As a result, the cooling effect for the models with $m_s = 150$ MeV becomes more significant compared with the models with $m_s = 200$ MeV. The high cooling rate induces the proto-neutron star contraction and increases the central temperature T_c. For example, the (150, 20) model shows $T_c \approx 30.8$ MeV at the post-bounce time $t_{pb} = 370$ ms, whereas the (200, 20) model shows $T_c \approx 25.5$ MeV. The increase in the mean energy is the most significant for heavy lepton neutrinos because ν_X interacts with the surrounding matter only through the neutral-current reactions and the radius of neutrinosphere is the smallest. This effect of the proto-neutron contraction is similar to that reported in supernova models with QCD axions [78].

Since we consider sterile neutrinos that decay into tau neutrinos, there is a contribution of the daughter neutrinos to the neutrino luminosity. Figure 8 shows the luminosities of the tau neutrinos produced by sterile neutrino decay, L_{decay}. In our parameter range, L_{decay} does not exceed the luminosity of tau neutrinos produced in the neutrinosphere, L_{SM}. Contrary to L_{SM}, L_{decay} increases as a function of the mixing
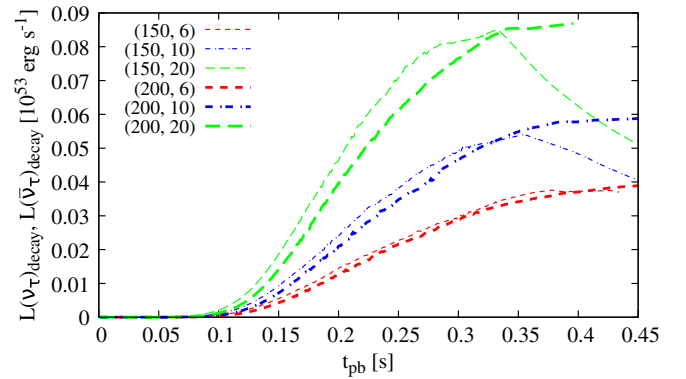

FIG. 8. The luminosity of decay tau (anti)neutrinos as a function of t_{pb}. The thin lines are for the models with $m_s = 150$ MeV and the thick lines are for the models with $m_s = 200$ MeV.
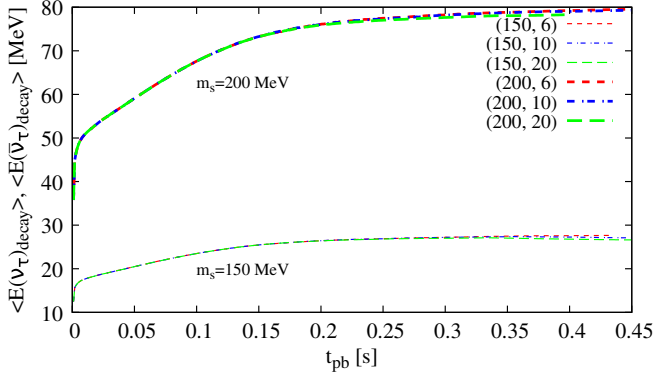
FIG. 9. The mean energy of decay tau (anti)neutrinos as a function of t_{pb}. The thin lines are for the models with $m_s = 150$ MeV and the thick lines are for the models with $m_s = 200$ MeV, as shown in the labels.

angle because larger mixing angles lead to higher sterile neutrino fluxes. Compared with the large difference in the sterile neutrino luminosity found in Fig. 2, the difference of L_{decay} between the models with different sterile neutrino masses is less significant. This is because the fraction of the sterile neutrino energy which is distributed to tau neutrinos is different. The fraction is given by $1 - x_{\gamma\gamma} \approx 9.5\%$ for $m_s = 150$ MeV and $\approx 27\%$ for $m_s = 200$ MeV. Thus, heavier sterile neutrinos give a larger fraction of their energy to tau neutrinos.

Since sterile neutrinos are heavier than the mean energies for active neutrinos, decay tau neutrinos can be more energetic than the main component of the supernova neutrino signal. Figure 9 shows the mean energy of decay neutrinos, which is denoted as $\langle E_{decay} \rangle$. One can see that $\langle E_{decay} \rangle$ is sensitive to the sterile neutrino mass. The mean energy reaches ~ 80 MeV when $m_s = 200$ MeV, whereas $\langle E_{decay} \rangle \sim 28$ MeV when $m_s = 150$ MeV. This behavior of the mean energy can be explained as follows. The average Lorentz factor for sterile neutrinos is estimated as [48,50]

$$\gamma = 1.3 \left(\frac{T}{35 \text{ MeV}} \right)^{0.4} \left(\frac{m_s}{200 \text{ MeV}} \right)^{-1}, \qquad (11)$$

where T is the temperature at the region where sterile neutrinos are produced. Thus, the mean energy of decay neutrinos can be roughly estimated as

$$\langle E_{decay} \rangle \approx \gamma m_s (1 - x_{\gamma\gamma}) \approx 130 \text{ MeV} \left(1 - \frac{m_\pi^2}{m_s^2} \right), \qquad (12)$$

where the weak temperature dependence is neglected. This expression shows that the mass dependence of $\langle E_{decay} \rangle$ originates from the kinematics of the sterile neutrino decay. We consider the detectability of this higher energy neutrino flux next.

TABLE II. The number of neutrino events N_{SM} integrated from $t_{pb} = 0$ s to 0.4 s from a supernova at $D = 8.5$ kpc observed by Hyper-Kamiokande. Here, neutrinos only from the neutrino-sphere are counted (see Table III for the contribution from sterile neutrino decays). We consider four cases for different treatments of the neutrino oscillation. In the "No Oscillation" case, oscillation is not implemented. In the "NH" and "IH" cases, the MSW effect is taken into account, assuming the normal and the inverted mass hierarchies, respectively. In the "Swap" case, the complete flavor swap between $\bar{\nu}_e$ and $\bar{\nu}_\tau$ is assumed.

Model	No Oscillation	NH	IH	Swap
Standard	30539	30698	31018	31030
(150, 6)	29666	30014	30714	30739
(150, 10)	29803	29981	30338	30350
(150, 20)	28436	28793	29513	29538
(200, 6)	29408	29774	30513	30539
(200, 10)	29142	29510	30251	30278
(200, 20)	27038	27851	29489	29547

D. Event number of decay neutrinos

Although the luminosity L_{decay} of decay neutrinos is lower than L_{SM}, their high mean energy for $m_s = 200$ MeV could lead to distinguishable signatures in neutrino signals from a nearby supernova event [48,51]. In this section, we estimate the electron antineutrino event number that could be detected by Hyper-Kamiokande [79,80].

The neutrino flux observed on Earth would be affected by neutrino oscillation during propagation in stellar matter and vacuum. However, neutrinos in a dense environment could experience complicated processes such as collective oscillation [e.g., [81–84]] and the collisional flavor instability [e.g., [85,86]], whose accurate treatment has not been established. We hence consider four phenomenological cases as shown in Tables II and III.

In the "No Oscillation" case, it is assumed that neutrinos do not oscillate during their propagation. In the normal hierarchy ("NH") and inverted hierarchy ("IH") cases, we consider the matter (Mikheyev–Smirnov–Wolfenstein, MSW) effect [87–89], assuming the normal and the inverted hierarchies for the active neutrino masses,

TABLE III. The same as Table II, but for the number of neutrino detections from sterile neutrino decay, N_{decay}.

Model	No Oscillation	NH	IH	Swap
Standard	0	0	0	0
(150, 6)	0	274	553	1588
(150, 10)	0	429	1045	2481
(150, 20)	0	705	1949	4077
(200, 6)	0	794	2196	4594
(200, 10)	0	1279	3533	7391
(200, 20)	0	2058	5686	11897

respectively. In the "Swap" case, we assume that the electron antineutrino flux on Earth is equal to the tau antineutrino flux on the neutrinosphere up to the geometrical factor.

The no oscillation case implies that the electron antineutrino flux on Earth is the same as the flux from the neutrinosphere up to the geometrical factor $1/D^2$, where D is the distance to the event. In the "NH" and "IH" cases, active neutrinos undergo flavor mixing induced by interactions with the surrounding matter during propagation. If we assume adiabaticity, this matter effect changes the neutrino flavors at the resonance density [e.g., [90,91]],

$$\rho_{\text{res}} = \frac{1}{2\sqrt{2}G_{\text{F}}} \frac{\Delta m^2}{E} \frac{m_{\text{N}}}{Y_e} \cos 2\theta$$
$$\approx 1.3 \times 10^2 \text{ g cm}^{-3}$$
$$\times \cos 2\theta \left(\frac{0.5}{Y_e}\right)\left(\frac{1 \text{ MeV}}{E}\right)\left(\frac{\Delta m^2}{10^{-5} \text{ eV}^2}\right), \quad (13)$$

where Δm^2 is a mass squared difference, E is the neutrino energy, m_{N} is the nucleon mass, Y_e is the electron mole fraction, and θ is a mixing angle. It follows that, for the H-resonance, $\rho_{\text{res}} \approx 3.9 \times 10^2$ g cm^{-3} for $m_{\text{s}} = 200$ MeV and $\rho_{\text{res}} \approx 1.1 \times 10^3$ g cm^{-3} for $m_{\text{s}} = 150$ MeV, assuming $E \approx \langle E_{\text{decay}}\rangle$. These densities correspond to the radius $r_{\text{res}} \approx 7.4 \times 10^4$ km for $m_{\text{s}} = 200$ MeV and $r_{\text{res}} \approx 5.3 \times 10^4$ km for $m_{\text{s}} = 150$ MeV. It then turns out that r_{res} is

longer than the mean free path λ_{s} of sterile neutrinos with $m_{\text{s}} = 200$ MeV, which is shown in Table I, whereas r_{res} can be shorter than λ_{s} when $m_{\text{s}} = 150$ MeV. Thus, in the case of the inverted mass hierarchy, almost all decay tau antineutrinos would undergo the H-resonance when $m_{\text{s}} = 200$ MeV, whereas a part of the decay antineutrinos can evade the H-resonance when $m_{\text{s}} = 150$ MeV. On the other hand, we do not consider the effect of the L-resonance because it does not affect the antineutrino sector [90,91].

Considering the above estimates, we calculate the electron antineutrino flux on the Earth as follows in the "NH" and "IH" cases. In the case of the normal mass hierarchy, tau antineutrinos do not experience the MSW resonance. The electron antineutrino flux on Earth can then be estimated as [92,93]

$$f(\bar{\nu}_e) = c_{12}^2 c_{13}^2 f_{\text{SM}}(\bar{\nu}_e) + s_{12}^2 c_{13}^2 (f_{\text{SM}}(\bar{\nu}_x) + s_{23}^2 f_{\text{decay}}(\bar{\nu}_\tau))$$
$$+ s_{13}^2 (f_{\text{SM}}(\bar{\nu}_y) + c_{23}^2 f_{\text{decay}}(\bar{\nu}_\tau))$$
$$\approx c_{12}^2 f_{\text{SM}}(\bar{\nu}_e) + s_{12}^2 (f_{\text{SM}}(\bar{\nu}_x) + s_{23}^2 f_{\text{decay}}(\bar{\nu}_\tau)), \quad (14)$$

where ν_x and ν_y are rotated basis defined as $(|\nu_e\rangle, |\nu_x\rangle, |\nu_y\rangle) = R_{23}^{-1}(\theta_{23})(|\nu_e\rangle, |\nu_\mu\rangle, |\nu_\tau\rangle)$, R_{23} is the rotation matrix in the 2–3 space, f_{SM} is the flux of neutrinos produced on the neutrinosphere, f_{decay} is the flux of decay neutrinos, and $c_{ij} = \cos\theta_{ij}$ and $s_{ij} = \sin\theta_{ij}$ for integers i and j. In the case of the inverted hierarchy,

$$f(\bar{\nu}_e) = s_{13}^2(f_{\text{SM}}(\bar{\nu}_e) + c_{23}^2 c_{13}^2 f_{\text{decay}}^{\text{out}}(\bar{\nu}_\tau)) + s_{12}^2 c_{13}^2(f_{\text{SM}}(\bar{\nu}_x) + s_{23}^2 f_{\text{decay}}^{\text{in}}(\bar{\nu}_\tau)$$
$$+ |-c_{12}s_{23} - s_{12}c_{23}s_{13}e^{i\delta}|^2 f_{\text{decay}}^{\text{out}}(\bar{\nu}_\tau)) + c_{12}^2 c_{13}^2(f_{\text{SM}}(\bar{\nu}_y) + c_{23}^2 f_{\text{decay}}^{\text{in}}(\bar{\nu}_\tau)$$
$$+ |s_{12}s_{23} - c_{12}c_{23}s_{13}e^{i\delta}|^2 f_{\text{decay}}^{\text{out}}(\bar{\nu}_\tau))$$
$$\approx s_{12}^2(f_{\text{SM}}(\bar{\nu}_x) + s_{23}^2 f_{\text{decay}}^{\text{in}}(\bar{\nu}_\tau) + c_{12}^2 s_{23}^2 f_{\text{decay}}^{\text{out}}(\bar{\nu}_\tau)) + c_{12}^2(f_{\text{SM}}(\bar{\nu}_y) + c_{23}^2 f_{\text{decay}}^{\text{in}}(\bar{\nu}_\tau) + s_{12}^2 s_{23}^2 f_{\text{decay}}^{\text{out}}(\bar{\nu}_\tau)), \quad (15)$$

where δ is the CP violation phase and $f_{\text{decay}}^{\text{in}}(\bar{\nu}_\tau)$ and $f_{\text{decay}}^{\text{out}}(\bar{\nu}_\tau)$ are the decay neutrino fluxes from the region where $r < r_{\text{res}}$ and $r > r_{\text{res}}$, respectively. In Eq. (15), we assume the incoherent vacuum oscillation of decay neutrinos produced at $r > r_{\text{res}}$.

Tables II and III show the electron antineutrino event numbers integrated over $t_{\text{pb}} = 0$–0.4 s observed by Hyper-Kamiokande through the inverse β-decay. Here we use $s_{12}^2 = 0.310$ and $s_{23}^2 = 0.558$ [94] and ignore the CP violation phase. We assume a supernova event at the Galactic Center, whose distance to the Solar System is $D = 8.5$ kpc. The volume of Hyper-Kamiokande is assumed to be 220 kt and the detection threshold neutrino energy is assumed to be 8.3 MeV. The spectrum of

neutrinos is fitted by a function [95],

$$f(E) = \frac{(1+\alpha)^{(1+\alpha)}}{\Gamma(1+\alpha)} \frac{E^\alpha}{\langle E\rangle^{\alpha+1}} \exp\left(-(1+\alpha)\frac{E}{\langle E\rangle}\right), \quad (16)$$

where $\alpha = (\langle E^2\rangle - 2\langle E\rangle)/(\langle E\rangle - \langle E^2\rangle)$, to estimate the number N_{SM} of neutrinos from the neutrinosphere. For the decay neutrino number N_{decay}, we treat decay neutrinos as monoenergetic particles with mean energy shown in Fig. 9.

The tables show that when the mixing angle is larger, N_{SM} becomes smaller because the active neutrino luminosity is decreased by sterile neutrinos. On the other hand, the contribution of decay neutrinos increases as the mixing angle
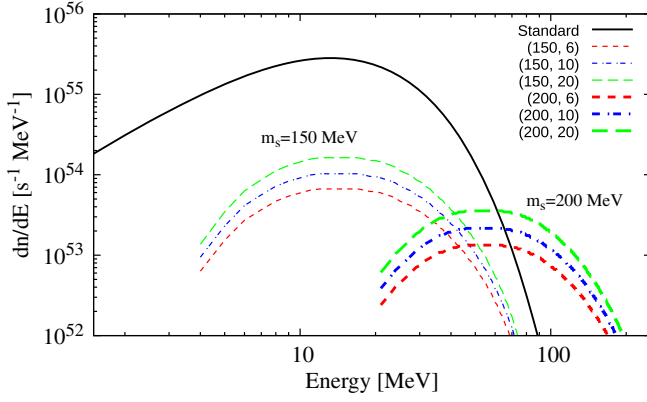
FIG. 10. The number spectra dn/dE of tau antineutrinos at $t_{pb} = 0.35$ s. The solid line shows the component produced on the neutrinosphere in the "Standard" model, and the broken lines show the contribution of decay antineutrinos. The thin lines are for the models with $m_s = 150$ MeV and the thick lines are for the models with $m_s = 200$ MeV, as shown in the labels.

FIG. 11. The neutrino event number observed by Hyper-Kamiokande as functions of the positron energy in 1 MeV bins, integrated over $t_{pb} = 0$–0.4 s. The supernova is assumed to be located at $D = 8.5$ kpc and the "Swap" case is adopted to take into account neutrino oscillations. The solid line shows the component produced on the neutrinosphere in the "Standard" model, and the broken lines show the contribution of decay antineutrinos in the models with $m_s = 200$ MeV.

becomes larger because of the higher sterile neutrino luminosity. Furthermore, the contribution of N_{SM} to the total neutrino event number is larger than N_{decay} in the parameter region discussed in this study. In the "No Oscillation" case, decay neutrinos cannot be detected using the inverse β decay because they are tau antineutrinos. On the other hand, the expected event number becomes the largest in the "Swap" case because all of the decay neutrinos are swapped with electron antineutrinos. Although the accurate treatment for the neutrino oscillation is not established, the "Swap" case works as an upper limit on the decay neutrino event number.

A key distinguishing feature of the decay neutrinos is its higher energy. As shown in Fig. 9, when $m_s = 200$ MeV, $\langle E_{decay} \rangle$ reaches 80 MeV, which is much higher than the mean energy of neutrinos from the neutrinosphere. This leads to a possibility that decay neutrinos could form a distinguishable bump in the neutrino spectrum [51]. Figure 10 shows the number spectra of tau antineutrinos that are produced by the sterile neutrino decay (shown in the broken lines) and standard processes (shown in the solid line) at $t_{pb} = 350$ ms. Here, instead of the fitting formula Eq. (3) used in the simulations to reduce computational cost, we evaluate the collisional integral in order to explore the spectra of decay neutrinos,

$$\mathcal{C}_{coll} = \frac{1}{2E_s} \int d^3\hat{p}_2 d^3\hat{p}_3 d^3\hat{p}_4 (1 - f_2) f_3 f_4$$
$$\times S|M|^2 \delta^{(4)}(p_s + p_2 - p_3 - p_4)(2\pi)^4, \quad (17)$$

where E_s is the sterile neutrino energy, p_s, p_2, p_3, and p_4 are the momenta of neutrinos involved in the reactions, f_2, f_3, and f_4 are the Fermi–Dirac distributions of active neutrinos, S is the symmetry factor, and $|M|^2$ is the amplitude tabulated in Refs. [48,51]. We adopt a reduction
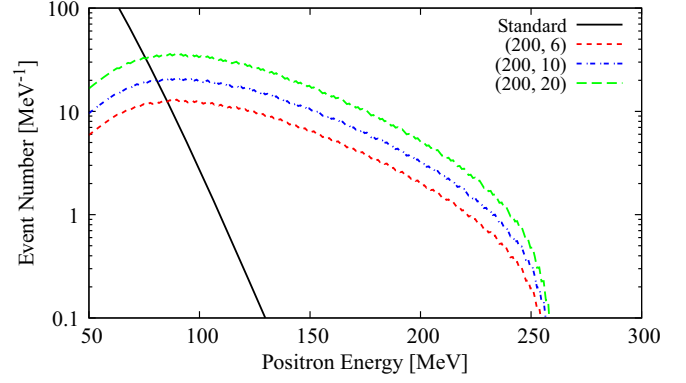
method developed in Refs. [96–98] to calculate the integral. We then estimate the decay neutrino spectrum as [51]

$$\frac{dn}{dE} = \frac{m_s}{2\bar{E}} \int_{E_{min}}^{\infty} dE_s \frac{1}{p_s} \frac{dn_s}{dE_s}, \quad (18)$$

where p_s is the sterile neutrino momentum, dn_s/dE_s is the sterile neutrino spectrum obtained from the collisional integral, $\bar{E} = (m_s^2 - m_\pi^2)/2m_s$, and $E_{min} = m_s(E^2 + \bar{E}^2)/2E\bar{E}$.

Figure 10 shows that decay antineutrinos form a high-energy bump at $E \sim 60$ MeV in the cases of $m_s = 200$ MeV, while the bump is located at $E \sim 20$ MeV in the $m_s = 150$ MeV cases. Although the total event number of the decay component observed by water-Cherenkov detectors will be smaller than the standard component as shown in Tables II and III, the bump could appear in the spectrum as a detectable high-energy component at $E \gtrsim 60$ MeV if $m_s \sim 200$ MeV. On the other hand, when sterile neutrinos are lighter, it would be difficult to distinguish the signals of decay neutrinos from the standard component.

Figure 11 shows the expected neutrino event number per 1 MeV observed by Hyper-Kamiokande as a function of the positron energy. The supernova event is assumed to be located at $D = 8.5$ kpc and the neutrino oscillation is treated with the "Swap" scheme, which gives an upper limit on the electron antineutrino flux on Earth. One can see that, if we adopt the energy bin width of ~ 10 MeV, the decay antineutrinos up to $E \sim 250$ MeV would be above the detection threshold. This implies that the high-energy tail of the neutrino spectrum will play a critical role in investigating a signature of sterile neutrinos. We note, however, that high-energy neutrinos could be produced nonthermally by shock acceleration even without sterile neutrinos [e.g., [99,100]]. Nevertheless, given the typically

power-law nature of nonthermal emission, the spectra could be a distinguishing feature. Since detailed studies on the shock acceleration with multidimensional supernova models have yet to be conducted, we leave a detailed comparison between the nonthermal component and the nonstandard decay component for future study.

E. Gravitational waves

Multidimensional supernova models have indicated that a nearby supernova event can be a source of gravitational waves (GWs; e.g., [91]), although they have not been detected yet. GWs can provide information on the supernova core because of their feeble interaction with matter.

In general, GWs can be decomposed into two modes, the plus mode and the cross mode. Axisymmetric models can only predict the plus mode. Figure 12 shows the strain of the GW plus mode observed from the equatorial direction. In all of the models, the amplitude of the GW strain h_+ is tiny until $t_{pb} \sim 0.15$ s because the mass accretion is spherically symmetric. However, it becomes larger after the phase because asymmetric motion behind the bounce shock starts growing. We can see that the strain becomes smaller when the mixing angle is larger. This is because the mass accretion on a proto-neutron star is
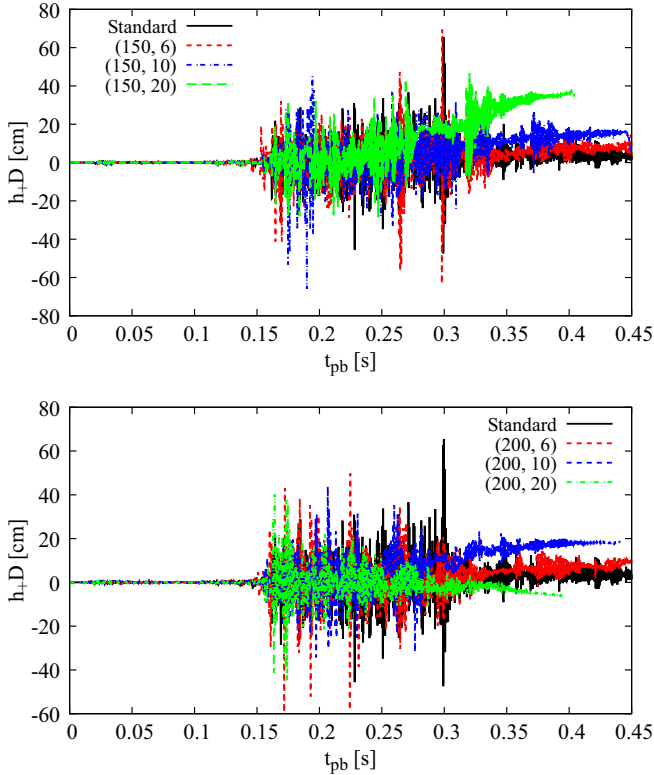

FIG. 12.   The strain h_+ of the gravitational wave (GW) plus mode times the distance D to the supernova event as a function of t_{pb}. The upper panel is for the models with $m_s = 150$ MeV and the lower panel is for the ones with $m_s = 200$ MeV. The solid line shows the result for the "Standard" model and the others are for the models with sterile neutrinos.
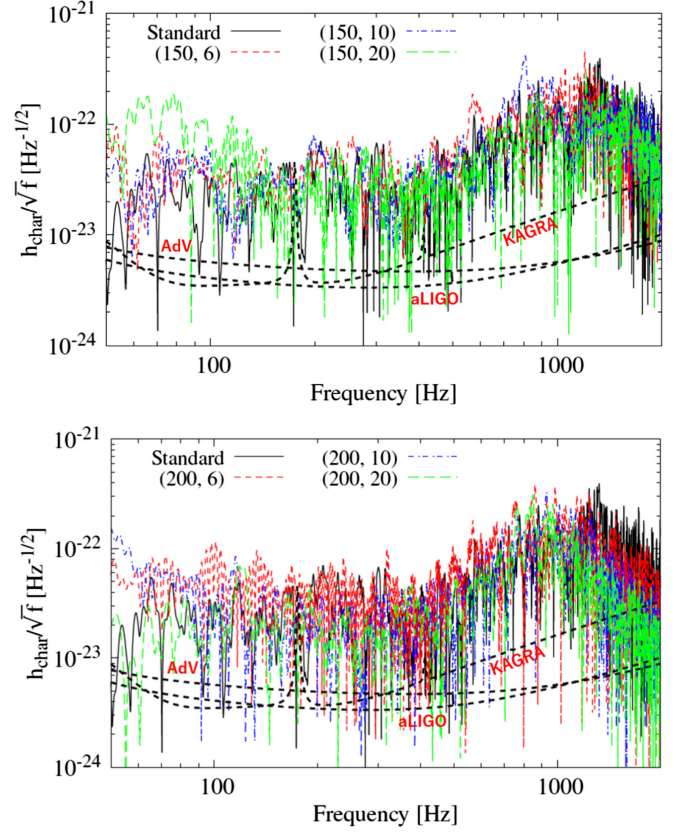

FIG. 13.   The characteristic GW strain defined in Eq. (19) divided by $\sqrt{f}$ from a supernova event at $D = 8.5$ kpc. Sensitivities of Advanced LIGO [102], Advanced VIRGO [103], and KAGRA [104] are also shown. The upper panel is for the models with $m_s = 150$ MeV and the lower panel is for the ones with $m_s = 200$ MeV. The solid line shows the result for the "Standard" model and the others are for the models with sterile neutrinos.

suppressed by the additional heating. Also, when the mixing angle is sufficiently large, the GW waveform deviates from 0. Except for the (200, 20) model, the strain maintains positive values. This memory effect can be attributed to the asymmetric expansion of matter [101]. The positive deviation implies a prolate explosion, whereas the negative deviation implies an oblate explosion. Since the matter tends to expand towards the polar direction, the explosion often becomes prolate.

Figure 13 shows the characteristic strain defined as

$$h_{char} = \sqrt{\frac{2}{\pi D^2} \frac{dE_{GW}}{df}}, \qquad (19)$$

where dE_{GW}/df is the GW spectral energy density. In this figure, D is fixed to 8.5 kpc. All models show a peak at $f \sim 1$ kHz. In a lower frequency region at $f \sim 100$ kHz, the (150, 20) model shows an enhancement compared with the other models. This is because the model produces the highest luminosity of sterile neutrinos, as shown in Fig. 2, and hence causes the most significant memory effect.
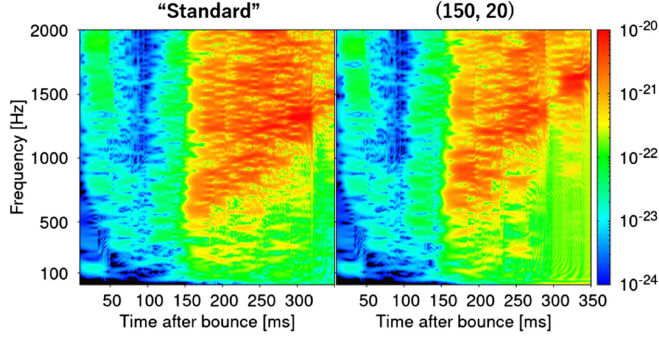
FIG. 14. The spectrograms for the "Standard" and (150, 20) models, where the color shows the value of $h_{\rm char}$. The supernova event is assumed to be located at $D = 8.5$ kpc.

Figure 13 shows the sensitivity of Advanced LIGO [102], Advanced VIRGO [103], and KAGRA [104] as well. It can be seen that the GW signals would be observable in our parameter range if a supernova event appears at the Galactic Center.

Figure 14 shows the spectrograms for the "Standard" and (150, 20) models. One can see that the two spectrograms are similar to each other and it would be difficult to distinguish them observationally. In general, the GW spectrum is dependent on the protoneutron star (PNS) mass and radius. However, the effects of sterile neutrinos are too small to cause qualitative differences in the GW spectrum in our parameter region.

IV. DISCUSSION

In this study, we performed two-dimensional simulations of stellar core collapse including the transport of heavy sterile neutrinos. We found that photons produced through the decay channel $\nu_s \to \nu_\tau \pi^0 \to \nu_\tau \gamma\gamma$ can heat the stellar material to enhance the explosion energy and the synthesized nickel mass. In addition, sterile neutrinos can suppress active neutrino and GW signals from a nearby supernova event, although they could be still observed if the event appears at the Galactic Center. Interestingly, the additional cooling induced by the sterile neutrino production led to the protoneutron star contraction and increased the active neutrino mean energy when $m_s = 150$ MeV. It was also found that decay tau neutrinos have higher mean energies than neutrinos from the neutrinosphere when $m_s = 200$ MeV. In this case, it would be possible to detect a high energy bump in neutrino spectra by, e.g., Hyper-Kamiokande, which would be a signature of sterile neutrinos.

It has been pointed out that one of the most useful observables to constrain feebly-interacting particles that are produced in supernovae is the explosion energy [67,105,106]. Since the explosion energy for our sterile neutrino models reaches $\sim 10^{51}$ erg and is still increasing at the end of the simulations, the sterile neutrino parameters with $\sin^2 \theta_{\tau 4} \gtrsim 1 \times 10^{-7}$ for $m_s \sim 150$–200 MeV would presumably be excluded. Recently, this argument was

applied to the explosion energies of low-energy supernova events to obtain tight constraints [52,53]. Although the parameter range in this study is in the excluded region based on the explosion energy, our prediction on multimessenger signals from a nearby supernova event would work as a method to obtain an independent constraint. Apart from the explosion energy, we showed the effects of sterile neutrinos on the thermal component of active neutrinos and GWs in Sec. III. Although the signals are slightly suppressed, their variations are within model uncertainties. We hence conclude that the high-energy bump in the neutrino spectrum and the enhanced explosion energy would be particularly useful for the search of heavy sterile neutrinos.

It is known that two- and three-dimensional supernova models can behave in qualitatively different ways [e.g., [61,107–112]], because turbulence cascades to small scales in three-dimensional models, whereas it cascades to large scales in two-dimensional models. In addition, two-dimensional models cannot predict the cross-mode of GWs. More sophisticated treatment of general relativity (GR) would be indispensable to obtain temperature of proto-neutron stars [111,113–115]. It is hence desirable to perform three-dimensional GR simulations that take sterile neutrinos into account to provide more accurate predictions. It would also be important to improve the transport scheme for sterile neutrinos. In our simulations, the transport is treated with the ray-by-ray approximation, in which sterile neutrinos propagate only in the radial direction. Although it could be computationally expensive, improving the transport scheme would lead to more accurate results.

Finally, in this study we have not taken into account detailed neutrino oscillation, e.g., fast flavor conversion [116–119] and collisional flavor instability [85]. Those flavor conversions may affect the neutrino heating rate and explodability of supernovae [120–123]. In strongly magnetized proto-neutron stars, spin-flavor precession would mix the flavors [124,125]. Neutrinos also may lead to chiral plasma instability [126–128]. These ingredients should be considered in the future to update the "Standard" model.

In summary, in this work we focused on heavy sterile neutrinos with $m_s \sim 200$ MeV in the context of core-collapse supernovae. However, the parameter space for the sterile neutrino particle is vast, and different masses can cause various phenomena in supernovae [24–45]. Such phenomenology has been investigated only with one-dimensional supernova models. Although one can estimate sterile neutrino luminosities from a supernova core with one-dimensional models, signatures of sterile neutrinos in multimessenger signals from supernova events cannot be predicted without multidimensional simulations. It is hence desirable to extend this study to a wider range of the parameter space to fully utilize supernovae as a laboratory for sterile neutrinos.

[1] S. Fukuda *et al.*, Phys. Rev. Lett. **85**, 3999 (2000).

[2] Q. R. Ahmad *et al.*, Phys. Rev. Lett. **87**, 071301 (2001).

[3] B. Pontecorvo, Sov. J. Exp. Theor. Phys. **26**, 984 (1968).

[4] B. Dasgupta and J. Kopp, Phys. Rep. **928**, 1 (2021).

[5] P. Minkowski, Phys. Lett. **67B**, 421 (1977).

[6] R. N. Mohapatra and G. Senjanovic, Phys. Rev. Lett. **44**, 912 (1980).

[7] T. Yanagida, Prog. Theor. Phys. **64**, 1103 (1980).

[8] P. Huber, Phys. Rev. C **84**, 024617 (2011).

[9] T. A. Mueller, D. Lhuillier, M. Fallot, A. Letourneau, S. Cormon, M. Fechner, L. Giot, T. Lasserre, J. Martino, G. Mention, A. Porta, and F. Yermia, Phys. Rev. C **83**, 054615 (2011).

[10] A. C. Hayes and P. Vogel, Annu. Rev. Nucl. Part. Sci. **66**, 219 (2016).

[11] G. Mention, M. Fechner, T. Lasserre, T. A. Mueller, D. Lhuillier, M. Cribier, and A. Letourneau, Phys. Rev. D **83**, 073006 (2011).

[12] S. Dodelson and L. M. Widrow, Phys. Rev. Lett. **72**, 17 (1994).

[13] X. Shi and G. M. Fuller, Phys. Rev. Lett. **82**, 2832 (1999).

[14] A. Boyarsky, M. Drewes, T. Lasserre, S. Mertens, and O. Ruchayskiy, Prog. Part. Nucl. Phys. **104**, 1 (2019).

[15] E. Bulbul, M. Markevitch, A. Foster, R. K. Smith, M. Loewenstein, and S. W. Randall, Astrophys. J. **789**, 13 (2014).

[16] A. Boyarsky, O. Ruchayskiy, D. Iakubovskyi, and J. Franse, Phys. Rev. Lett. **113**, 251301 (2014).

[17] A. Boyarsky, J. Franse, D. Iakubovskyi, and O. Ruchayskiy, Phys. Rev. Lett. **115**, 161301 (2015).

[18] S. Horiuchi, P. J. Humphrey, J. Onorbe, K. N. Abazajian, M. Kaplinghat, and S. Garrison-Kimmel, Phys. Rev. D **89**, 025017 (2014).

[19] K. N. Abazajian, Phys. Rev. Lett. **112**, 161303 (2014).

[20] A. C. Hayes, J. L. Friar, G. T. Garvey, G. Jungman, and G. Jonkmans, Phys. Rev. Lett. **112**, 202501 (2014).

[21] S. Horiuchi, B. Bozek, K. N. Abazajian, M. Boylan-Kolchin, J. S. Bullock, S. Garrison-Kimmel, and J. Onorbe, Mon. Not. R. Astron. Soc. **456**, 4346 (2016).

[22] C. Dessert, N. L. Rodd, and B. R. Safdi, Science **367**, 1465 (2020).

[23] B. M. Roach, S. Rossland, K. C. Y. Ng, K. Perez, J. F. Beacom, B. W. Grefenstette, S. Horiuchi, R. Krivonos, and D. R. Wik, Phys. Rev. D **107**, 023009 (2023).

[24] K. Kainulainen, J. Maalampi, and J. T. Peltoniemi, Nucl. Phys. **B358**, 435 (1991).

[25] J. T. Peltoniemi, Astron. Astrophys. **254**, 121 (1992).

[26] G. Raffelt and G. Sigl, Astropart. Phys. **1**, 165 (1993).

[27] H. Nunokawa, J. T. Peltoniemi, A. Rossi, and J. W. F. Valle, Phys. Rev. D **56**, 1704 (1997).

[28] G. C. McLaughlin, J. M. Fetter, A. B. Balantekin, and G. M. Fuller, Phys. Rev. C **59**, 2873 (1999).

[29] D. O. Caldwell, G. M. Fuller, and Y.-Z. Qian, Phys. Rev. D **61**, 123005 (2000).

[30] J. Fetter, G. C. McLaughlin, A. B. Balantekin, and G. M. Fuller, Astropart. Phys. **18**, 433 (2003).

[31] J. Beun, G. C. McLaughlin, R. Surman, and W. R. Hix, Phys. Rev. D **73**, 093007 (2006).

[32] P. Keränen, J. Maalampi, M. Myyryläinen, and J. Riittinen, Phys. Rev. D **76**, 125026 (2007).

[33] I. Tamborra, G. G. Raffelt, L. Hüdepohl, and H.-T. Janka, J. Cosmol. Astropart. Phys. 01 (2012) 013.

[34] M.-R. Wu, T. Fischer, L. Huther, G. Martínez-Pinedo, and Y.-Z. Qian, Phys. Rev. D **89**, 061303 (2014).

[35] X. Shi and G. Sigl, Phys. Lett. B **323**, 360 (1994).

[36] K. Abazajian, G. M. Fuller, and M. Patel, Phys. Rev. D **64**, 023501 (2001).

[37] J. Hidaka and G. M. Fuller, Phys. Rev. D **74**, 125015 (2006).

[38] J. Hidaka and G. M. Fuller, Phys. Rev. D **76**, 083516 (2007).

[39] G. G. Raffelt and S. Zhou, Phys. Rev. D **83**, 093014 (2011).

[40] M. L. Warren, M. Meixner, G. Mathews, J. Hidaka, and T. Kajino, Phys. Rev. D **90**, 103007 (2014).

[41] M. L. Warren, G. J. Mathews, M. Meixner, J. Hidaka, and T. Kajino, Int. J. Mod. Phys. A **31**, 1650137 (2016).

[42] C. A. Argüelles, V. Brdar, and J. Kopp, Phys. Rev. D **99**, 043012 (2019).

[43] A. M. Suliga, I. Tamborra, and M.-R. Wu, J. Cosmol. Astropart. Phys. 12 (2019) 019.

[44] A. M. Suliga, I. Tamborra, and M.-R. Wu, J. Cosmol. Astropart. Phys. 08 (2020) 018.

[45] V. Syvolap, O. Ruchayskiy, and A. Boyarsky, Phys. Rev. D **106,** 015017 (2022).

[46] A. Ray and Y.-Z. Qian, Phys. Rev. D **108,** 063025 (2023).

[47] A. D. Dolgov, S. H. Hansen, G. Raffelt, and D. V. Semikoz, Nucl. Phys. **B590,** 562 (2000).

[48] G. M. Fuller, A. Kusenko, and K. Petraki, Phys. Lett. B **670,** 281 (2009).

[49] C. Albertus, M. Masip, and M. A. Pérez-García, Phys. Lett. B **751,** 209 (2015).

[50] T. Rembiasz, M. Obergaulinger, M. Masip, M. A. Pérez-García, M. A. Aloy, and C. Albertus, Phys. Rev. D **98,** 103010 (2018).

[51] L. Mastrototaro, A. Mirizzi, P. D. Serpico, and A. Esmaili, J. Cosmol. Astropart. Phys. 01 (2020) 010.

[52] G. Chauhan, S. Horiuchi, P. Huber, and I. M. Shoemaker, arXiv:2309.05860.

[53] P. Carenza, G. Lucente, L. Mastrototaro, A. Mirizzi, and P. D. Serpico, Phys. Rev. D **109,** 063010 (2024).

[54] K. Akita, S. H. Im, M. Masud, and S. Yun, arXiv:2312.13627.

[55] A. V. Artamonov et al. (E949 Collaboration), Phys. Rev. D **91,** 052001 (2015).

[56] E. Cortina Gil et al. (NA62 Collaboration), Phys. Lett. B **778,** 137 (2018).

[57] K. Abe, R. Akutsu, A. Ali, C. Andreopoulos, L. Anthony, M. Antonova, S. Aoki, A. Ariga, Y. Ashida, Y. Awataguchi et al., Phys. Rev. D **100,** 052006 (2019).

[58] R. L. Workman et al. (Particle Data Group), Prog. Theor. Exp. Phys. **2022,** 083C01 (2022).

[59] T. Takiwaki, K. Kotake, and Y. Suwa, Mon. Not. R. Astron. Soc. **461,** L112 (2016).

[60] M. Liebendörfer, S. C. Whitehouse, and T. Fischer, Astrophys. J. **698,** 1174 (2009).

[61] T. Takiwaki, K. Kotake, and Y. Suwa, Astrophys. J. **786,** 83 (2014).

[62] K. Kotake, T. Takiwaki, T. Fischer, K. Nakamura, and G. Martínez-Pinedo, Astrophys. J. **853,** 170 (2018).

[63] K. Nakamura, T. Takiwaki, K. Kotake, and N. Nishimura, Astrophys. J. **782,** 91 (2014).

[64] J. M. Lattimer and D. F. Swesty, Nucl. Phys. A **535,** 331 (1991).

[65] S. E. Woosley and A. Heger, Phys. Rep. **442,** 269 (2007).

[66] L. Martinez et al., Astron. Astrophys. **660,** A41 (2022).

[67] A. Sung, H. Tu, and M.-R. Wu, Phys. Rev. D **99,** 121305 (2019).

[68] K. Mori, T. Takiwaki, K. Kotake, and S. Horiuchi, Phys. Rev. D **108,** 063027 (2023).

[69] M. Ugliano, H.-T. Janka, A. Marek, and A. Arcones, Astrophys. J. **757,** 69 (2012).

[70] O. Pejcha and T. A. Thompson, Astrophys. J. **801,** 90 (2015).

[71] Y. Suwa, N. Tominaga, and K. Maeda, Mon. Not. R. Astron. Soc. **483,** 3607 (2019).

[72] R. Sawada and Y. Suwa, Astrophys. J. **908,** 6 (2021).

[73] W. D. Arnett, Astrophys. J. **253,** 785 (1982).

[74] S. E. Woosley, Astrophys. J. **330,** 218 (1988).

[75] J. P. Anderson, Astron. Astrophys. **628,** A7 (2019).

[76] H. Nagakura, A. Burrows, and D. Vartanyan, Mon. Not. R. Astron. Soc. **506,** 1462 (2021).

[77] Y. Suwa, A. Harada, M. Harada, Y. Koshio, M. Mori, F. Nakanishi, K. Nakazato, K. Sumiyoshi, and R. A. Wendell, Astrophys. J. **934,** 15 (2022).

[78] A. Betranhandy and E. O'Connor, Phys. Rev. D **106,** 063019 (2022).

[79] K. Abe et al. (Hyper-Kamiokande Proto-Collaboration), arXiv:1805.04163.

[80] K. Abe et al. (Hyper-Kamiokande Collaboration), Astrophys. J. **916,** 15 (2021).

[81] A. B. Balantekin and H. Yüksel, New J. Phys. **7,** 51 (2005).

[82] H. Duan, G. M. Fuller, J. Carlson, and Y.-Z. Qian, Phys. Rev. Lett. **97,** 241101 (2006).

[83] H. Duan, G. M. Fuller, and Y.-Z. Qian, Annu. Rev. Nucl. Part. Sci. **60,** 569 (2010).

[84] A. Mirizzi, I. Tamborra, H. T. Janka, N. Saviano, K. Scholberg, R. Bollig, L. Hüdepohl, and S. Chakraborty, Nuovo Cimento Riv. Ser. **39,** 1 (2016).

[85] L. Johns, Phys. Rev. Lett. **130,** 191001 (2023).

[86] J. Liu, H. Nagakura, R. Akaho, A. Ito, M. Zaizen, and S. Yamada, Phys. Rev. D **108,** 123024 (2023).

[87] L. Wolfenstein, Phys. Rev. D **20,** 2634 (1979).

[88] S. P. Mikheev and A. I. Smirnov, Nuovo Cimento C Geophys. Space Phys. C **9,** 17 (1986).

[89] H. A. Bethe, Phys. Rev. Lett. **56,** 1305 (1986).

[90] A. S. Dighe and A. Y. Smirnov, Phys. Rev. D **62,** 033007 (2000).

[91] K. Kotake, K. Sato, and K. Takahashi, Rep. Prog. Phys. **69,** 971 (2006).

[92] M.-R. Wu, Y.-Z. Qian, G. Martínez-Pinedo, T. Fischer, and L. Huther, Phys. Rev. D **91,** 065016 (2015).

[93] H. Sasaki, T. Takiwaki, S. Kawagoe, S. Horiuchi, and K. Ishidoshiro, Phys. Rev. D **101,** 063027 (2020).

[94] I. Esteban, M. C. Gonzalez-Garcia, A. Hernandez-Cabezudo, M. Maltoni, and T. Schwetz, J. High Energy Phys. 01 (2019) 106.

[95] M. T. Keil, G. G. Raffelt, and H.-T. Janka, Astrophys. J. **590,** 971 (2003).

[96] W. R. Yueh and J. R. Buchler, Astrophys. Space Sci. **39,** 429 (1976).

[97] S. Hannestad and J. Madsen, Phys. Rev. D **52,** 1764 (1995).

[98] L. Mastrototaro, P. D. Serpico, A. Mirizzi, and N. Saviano, Phys. Rev. D **104,** 016026 (2021).

[99] P. M. Giovanoni, D. C. Ellison, and S. W. Bruenn, Astrophys. J. **342,** 416 (1989).

[100] H. Nagakura and K. Hotokezaka, Mon. Not. R. Astron. Soc. **502,** 89 (2021).

[101] J. W. Murphy, C. D. Ott, and A. Burrows, Astrophys. J. **707,** 1173 (2009).

[102] L. Barsotti, S. Gras, M. Evans, and P. Fritschel, Report No. LIGO-T1800044, 2018.

[103] KAGRA, LIGO Scientific, and Virgo Collaborations, Report No. LIGO-P1200087-v48, 2019.

[104] K. Komori, Y. Michimura, and K. Somiya, Report No. JGW-T1707038, 2017.

[105] K. Mori, T. Takiwaki, K. Kotake, and S. Horiuchi, Phys. Rev. D **105,** 063009 (2022).

[106] A. Caputo, H.-T. Janka, G. Raffelt, and E. Vitagliano, Phys. Rev. Lett. **128,** 221103 (2022).

[107] S. M. Couch and E. P. O'Connor, Astrophys. J. **785,** 123 (2014).

[108] B. Müller, T. Melson, A. Heger, and H.-T. Janka, Mon. Not. R. Astron. Soc. **472,** 491 (2017).

[109] C. D. Ott, L. F. Roberts, A. da Silva Schneider, J. M. Fedrow, R. Haas, and E. Schnetter, Astrophys. J. Lett. **855,** L3 (2018).

[110] A. Burrows, D. Radice, D. Vartanyan, H. Nagakura, M. A. Skinner, and J. C. Dolence, Mon. Not. R. Astron. Soc. **491,** 2715 (2020).

[111] T. Kuroda, A. Arcones, T. Takiwaki, and K. Kotake, Astrophys. J. **896,** 102 (2020).

[112] R. Bollig, N. Yadav, D. Kresse, H.-T. Janka, B. Müller, and A. Heger, Astrophys. J. **915,** 28 (2021).

[113] B. Müller, H.-T. Janka, and H. Dimmelmeier, Astrophys. J. Suppl. Ser. **189,** 104 (2010).

[114] N. Rahman, H. T. Janka, G. Stockinger, and S. E. Woosley, Mon. Not. R. Astron. Soc. **512,** 4503 (2022).

[115] T. Kuroda and M. Shibata, Mon. Not. R. Astron. Soc. **526,** 152 (2023).

[116] I. Tamborra and S. Shalgar, Annu. Rev. Nucl. Part. Sci. **71,** 165 (2021).

[117] F. Capozzi and N. Saviano, Universe **8,** 94 (2022).

[118] S. Richers and M. Sen, arXiv:2207.03561.

[119] M. C. Volpe, arXiv:2301.11814.

[120] Y. Suwa, K. Kotake, T. Takiwaki, M. Liebendörfer, and K. Sato, Astrophys. J. **738,** 165 (2011).

[121] J. Ehring, S. Abbar, H.-T. Janka, G. Raffelt, and I. Tamborra, Phys. Rev. D **107,** 103034 (2023).

[122] J. Ehring, S. Abbar, H.-T. Janka, G. Raffelt, and I. Tamborra, Phys. Rev. Lett. **131,** 061401 (2023).

[123] H. Nagakura, Phys. Rev. Lett. **130,** 211401 (2023).

[124] H. Sasaki and T. Takiwaki, Phys. Rev. D **104,** 023018 (2021).

[125] H. Sasaki, T. Takiwaki, and A. B. Balantekin, Phys. Rev. D **108,** 103046 (2023).

[126] Y. Masada, K. Kotake, T. Takiwaki, and N. Yamamoto, Phys. Rev. D **98,** 083018 (2018).

[127] J. Matsumoto, N. Yamamoto, and D.-L. Yang, Phys. Rev. D **105,** 123029 (2022).

[128] K. Kamada, N. Yamamoto, and D.-L. Yang, Prog. Part. Nucl. Phys. **129,** 104016 (2023).